Chemical Engineering Science 292 (2024) 119934

Contents lists available at ScienceDirect

Chemical Engineering Science

journal homepage: www.elsevier.com/locate/ces

Modelling of iron oxide reduction with hydrogen in a small fixed bed

Emiliano Salucci [a,b,*], Antonio D'Angelo [a], Vincenzo Russo [b], Henrik Grénman [a], Henrik Saxén [a]

[a] Åbo Akademi University, Henrikinkatu 2, Turku 20500, Finland
[b] University of Naples Federico II, Via Cintia 26, Napoli 80126, Italy

ARTICLE INFO

Keywords:
Hydrogen
Iron oxides
Reduction experiments
Direct reduced iron
Green ironmaking
Kinetic modeling

ABSTRACT

The need to reduce the environmental impact of the steel industry necessitates the development of new production routes that drastically reduce the emissions of carbon dioxide. A potential solution is to change the reductant from carbon monoxide to hydrogen. In the development of such new ironmaking technologies, it is important to understand the iron oxide reduction kinetics under the novel conditions. In this work, a mathematical model of a small fixed-bed reactor was developed using the key assumptions of the Shrinking Core Model to describe the kinetics of the reactive network and mass transport phenomena involved. The model was found to be robust and to perform in a consistent way when subjected to changes in the model parameters and conditions. It was demonstrated to qualitatively reproduce the results of reduction experiments in a small-scale laboratory reactor. Preliminary analysis indicated a promising potential to adapt the model quantitatively to experimental results.

1. Introduction

Steelmaking is one of the most significant contributors to global CO_2 emissions, accounting for 2.6 Gt/a, which represents approximately 8 % of the direct global emissions (Energy Agency, 2020). Traditionally, the production of iron and steel begins in the blast furnace (BF), where iron ores (i.e., iron oxides) and coke (obtained by dry distillation of metallurgical coal) are alternately charged from above, while preheated air is blown into the lower part. Partial oxidation of the coke in the lower parts of the furnace produces large amounts of CO, which acts as a reducing agent in the gas. The reactions that occur in series in the furnace due to the presence of CO gradually remove oxygen from the iron oxides, which eventually, due to the high temperatures yield molten iron and slag (as a by-product), and a partially oxidized gas (Hutny et al., 1991). The molten iron, also called hot metal, is tapped out in the lower part of the furnace together with slag and is converted into steel in the downstream basic oxygen furnace process, while the gases leave the furnace at the top. It should be noted that the blast furnace cannot operate without coke as this burden material provides permeability to the bed and acts as a support in the lower part of the BF, where the ores have melted.

As an alternative to the BF, the Midrex direct reduction process was introduced 40 years ago, utilizing natural gas instead of coal. Syngas, produced by reforming natural gas, is used as a reducing gas mixture of primarily H_2 and CO. Under these conditions, Direct Reduced Iron (DRI) is produced by gas–solid reactions (Atsushi et al., 2010). Some of the advantages of this process over the BF are the lower operating temperatures and the absence of molten phases. However, the DRI produced must be melted in a separate vessel, traditionally an electric arc furnace. To decarbonize the iron and steel industry, an option is to use green hydrogen H_2 in the reducing gases in the DR furnace, eliminating the carbonaceous sources (Patisson et al., 2021) and green electricity in the melter.

Over the past 60 years, the scientific community has largely focused on studying the reduction of iron oxides by CO or CO-H_2 mixtures (Jess and Depner, 1998, Rahmatmand et al., 2023). The reason is obvious: in the BF, which still today represents the dominant ironmaking technology in the world, the reduction gas is primarily CO with smaller concentrations of H_2. More recently, because of the pressing need to reduce CO_2 emissions in iron and steelmaking, hydrogen reduction has attracted more attention (Spreitzer & Schenk, 2019). The reduction behavior of iron oxides in hydrogen-containing gases is still not sufficiently known, and more detailed studies of the kinetics should be undertaken. From a thermodynamic point of view, both the reduction in the presence of CO and in the presence of H_2 can be analyzed using the well-known Baur-Glässner or Chaudron diagram in Fig. 1, in which the temperature is shown on the ordinate and the Gas Oxidation Degree (GOD) on the abscissa (Bale et al., 2016 FactSage 8.2).

The GOD represents the ratio between the oxidizing species (CO_2 or H_2O) and the sum of the gaseous components (oxidant and reductant), i.

* Corresponding author.
E-mail address: emiliano.salucci@abo.fi (E. Salucci).

https://doi.org/10.1016/j.ces.2024.119934
Received 24 November 2023; Received in revised form 19 February 2024; Accepted 24 February 2024
Available online 26 February 2024

Notation

Abbreviations

BF	Blast Furnace
CFD	Computational Fluid Dynamic
GOD	Gas Oxidant Degree
DRI	Direct Reduction Iron
SCM	Shrinking core model

Symbols

A_j	Kinetic reaction resistance [s/m]
a_j	Proportional oxygen content parameter [–]
B_j	Intraparticle diffusion resistance [s/m]
C	Model variable state (X_j [–] or c_i [mol/m^3])
c_i	Concentration *i:*th gas in the reactor [mol/m^3]
$c_{i,\text{in}}$	Feed *i:*th gas concentration [mol/m^3]
D_z	Axial dispersion coefficient [m^2/s]
D_j	Intraparticle diffusion coefficient *j:*th reaction front [m^2/s]
$d_{1,j}$	First coefficient empirical interparticle diffusion equation [m^2/s]
$d_{2,j}$	Second coefficient empirical interparticle diffusion equation [–]
$d_{3,j}$	Third coefficient empirical interparticle diffusion equation [K]
$E_{a,j}$	Activation energy *j:*th reaction front [J/mol]
F	External diffusion resistance [s/m]
$g_{1,i}$	First coefficient in empirical thermal conductivity equation [W/(m K)]
$g_{2,i}$	Second coefficient in empirical thermal conductivity equation [–]
$g_{3,i}$	Third coefficient in empirical thermal conductivity equation [–]
$g_{4,i}$	Fourth coefficient in empirical thermal conductivity [–]
H	External diffusion coefficient [m/s]
h	Height of the solid bed [m]
K_j	Equilibrium constant *j:*th reaction front [–]
k_j	Kinetic constant *j:*th reaction front [m/s]
$k_{j,\text{ref}}$	Pre-exponential kinetic factor *j:*th reaction front [m/s]
m_O	Iron oxide initial mass [g]
N_j	Effective reaction SCM term ($f=1$ [–], $f=2$ [s^2/m^2], $f=3$ [s^3/m^3])
n	Number of parameters [–]
n_O	Initial concentration of oxygen [mol/m^3]
P	Operating pressure [N/m^2]
R	Ideal gas constant [J/(K mol)]
r_0	Iron oxide particle radius [m]
r_j	Reduction rate SCM [mol/(m^3 s)]
T	Operating temperature [K]
t	Time [s]
t_v	Number of time points [–]
u	Gas velocity [m/s]
W	Total resistance ($f=1$ [–]) ($f=2$ [s^2/m^2]) ($f=3$ [s^3/m^3])
X_j	Reduction degree *j:*th reaction front [–]
$y_{i,j}$	Gas molar fraction *i:*th species of *j:*th reaction front [–]
$d_{\text{H}_2,j,\text{eq}}$	Equilibrium molar fraction of H_2 of *j:*th reaction front [–]
z	Reactor axial coordinate [–]
z_v	Number of spatial grid points [–]
Δ	Parametric perturbation
ΔG_j	Gibbs free energy changes *j:*th reaction front [J/mol]
ΔH_j	Enthalpy changes *j:*th reaction front [J/mol]
ΔS_j	Entropy changes *j:*th reaction front [J/mol]
Δt	Maximum integration step
ε	Bed void degree [–]
λ_i	Gas thermal conductivity [W/(m K)]
$\nu_{i,j}$	Stoichiometric matrix [–]

Subscripts

f	Number of available reaction fronts
i	Gas species
j	Reaction fronts
l	Index in space vector
m	Index in parameter vector
p	Model parameter
s	Index in time vector
v	Space or time vector length

Superscripts

χ	Index of state variables [–]

e., it indicates the mole fraction of the oxidation agent in the system for each individual reaction. The crucial information that can be obtained from the diagram relates to the stability ranges of the different iron oxides at different operating temperatures in relation to the reduction driving forces. In the presence of CO, H_2, or both, at temperatures above 843 K, the reduction process undergoes three reversible reactions in series. Starting from the reduction of hematite (Fe_2O_3), the most abundant iron ore in nature, it passes through magnetite (Fe_3O_4) and wüstite (FeO) eventually producing metallic iron (Fe). In case of operating temperatures below 843 K, the reaction to FeO does not occur due to its instability, so the magnetite converts directly to iron (Zhang et al., 2013).

The main experimental approaches to study this reduction use thermogravimetric systems (Oh & Noh, 2017) or packed oxide beds (Chen et al., 2018) in contact with H_2 evaluating the reaction in terms of sample weight loss or analysis of the composition of the exhaust gases. The most commonly studied operating parameters for reduction kinetics are temperature (El-Geassy et al., 1996, Bernasowski, 2014), reducing gas composition (molar ratio of H_2 and inert gas) (Wei et al., 2018), and its volumetric flow rate (Hou et al., 2012). The study of the morphology and composition of the solid material to evaluate the state of the initial material (composition, structure, etc.) and the products as well as the different reaction steps are important elements (Gao et al., 1993). Many authors have evaluated the dependence of the reaction progress on the size and geometry of the mineral (e.g., minerals in brick or spherical shape) (Hou et al., 2012, Bonalde et al., 2005) or on its porosity (El-Geassy & Nasr, 1988). The main mathematical model used to describe the reduction process and estimate the kinetic parameters has been the *Avrami* model, but it has significant limitations (Piotrowski et al., 2005). Many other modeling approaches have been reported in the literature, such as the Shrinking Core Model (Zuo et al., 2015), the Grain Model (Bonalde et al., 2005), or the Random Pore Model (Szekely & Evans, 1970). Mathematical models have also been developed to address the study of reduction supported by the fluid dynamic analysis of the gas/solid system using Computational Fluid Dynamics modeling (*CFD*) at both laboratory scale (Kazemi et al., 2017) and furnace scale (Mauret et al., 2023). However, the findings are inconclusive since many different rate-limiting steps have been reported, including intraparticle diffusion, kinetics, or mixed counterparts depending on the experimental conditions or the reduction steps studied (Lin et al., 2003). Furthermore, the experimental and theoretical approaches have resulted in a large scattering of kinetic coefficients. For instance, reported activation energy values estimated for all individual reactions or for the whole reduction process vary widely between 18 kJ/mol and 246 kJ/

mol (Pineau et al., 2006). The main reason for this lies in the different experimental approaches (Hammam et al., 2021), and in the key properties of the solid and the reducing gases. In several works, the sample used for the evaluation of the kinetic parameters contained a high proportion of gangue (Chen et al., 2015) while it in other studies was prepared in situ in the laboratory with high purity (Jozwiak et al., 2007). The shape and dimensions of the particles as well as their physical properties, including porosity and density, also varied (El-Geassy & Nasr, 1988) making the assessment of the accuracy of the reported activation energies difficult. For this reason, it is not possible to determine the parameters of the intrinsic kinetics based on what has been reported in the literature (Spreitzer & Schenk, 2019). In order to provide a solid framework for a systematic study of the reduction kinetics of iron oxides with H_2, this work proposes a mathematical model capable of describing the system in its complexity by evaluating both kinetic and mass transfer phenomena of the reduction of iron oxides in a small fixed bed. The goal of the model is to act as a tool by which kinetic parameters can be estimated based on results from small-scale reduction experiments, which is a prerequisite for of a model-based analysis of new direct reduction processes of iron ore using hydrogen.

2. Materials and methods

2.1. Mathematical model

The mathematical model developed in this study includes the description of the reaction network for the reduction of iron oxide in the presence of H_2. The reactor system studied consists of a fixed bed of iron oxide fines through which a reducing gas flow. The operating conditions imply the need to evaluate the kinetic, thermodynamic, and diffusive intra- and interparticle phenomena. Table 1 shows the system of reversible chemical reactions relevant in the system.

The reactive and diffusive intraparticle phenomena can be described in detail by the Shrinking Core Model (Hara et al., 1974), which is based on a series of implicit assumptions:

Table 1
Reaction network. Enthalpy values taken from (Zhang et al., 2013).

Reaction fronts (j)	Reduction reaction	ΔH^0[kJ/mol]
1	$3Fe_2O_3 + H_2 \Leftrightarrow 2Fe_3O_4 + H_2$	−2
2	$Fe_3O_4 + H_2 \Leftrightarrow 3FeO + H_2O$	+ 89
3	$FeO + H_2 \Leftrightarrow Fe + H_2O$	+ 25
4*	$Fe_3O_4 + 4H_2 \Leftrightarrow 3Fe + 4H_2O$	+ 38

* Reaction 4 replaces reactions 2 and 3 if the operating temperature is lower than 843 K.

i. solid structure and porosity of the different solid layers are radially homogeneous;
ii. constant total gas concentration inside the particle (if the temperature and pressure of the gas in the particle are uniform);
iii. diffusion flux described by Fick's law with constant effective diffusivity;
iv. quasi-stationary state of the gas (i.e., no accumulation of gas species).

The main explicit assumption of the SCM is that the reaction occurs exclusively at surfaces that characterize the separation between distinct zones of the solid, an unreacted core and a reacted outer layer. The surface area of this reaction front decreases as the reaction progresses (i.e., as the core is consumed). Given the reactive network studied in this work, it is necessary to account for three different reaction fronts. Fig. 2 provides a schematic description of the reactor system and the proposed three-front reaction SCM model.

2.2. Solid mass balance

To describe the degree of reduction of different oxides, differential mass balance equations were implemented in the model over time (t) and along the axial coordinate of the reactor (z)

$$\frac{\partial X_j(t,z)}{\partial t} = \frac{r_j(t,z)}{n_0 \cdot a_j} \tag{1}$$

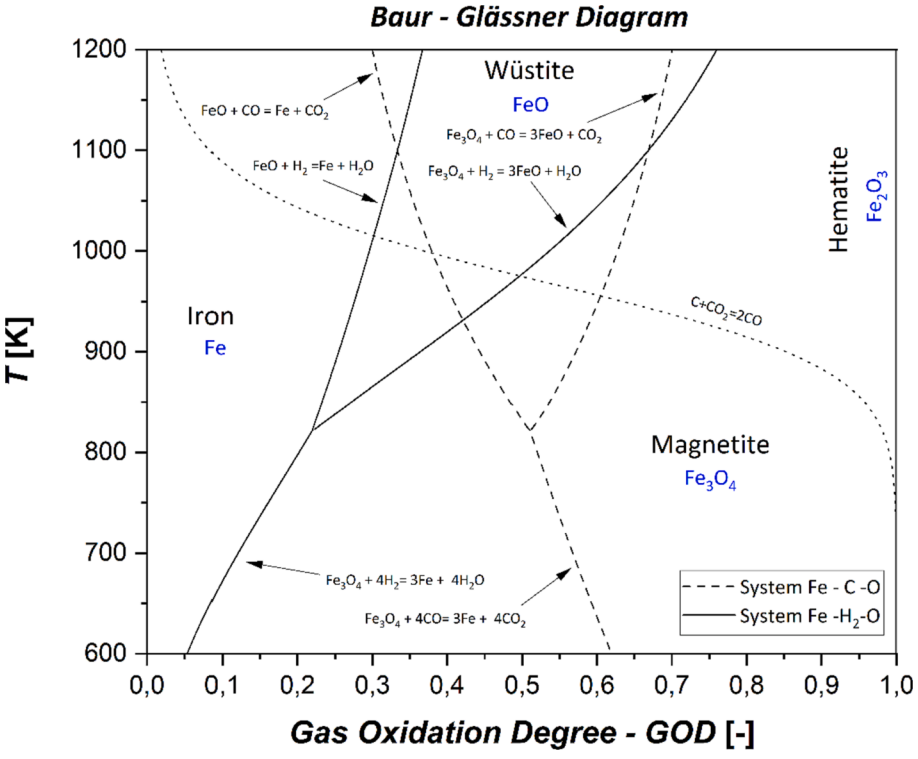

Fig. 1. Baur–Glässner/Chaudron thermodynamic diagram (Bale et al., 2016 FactSage 8.2).

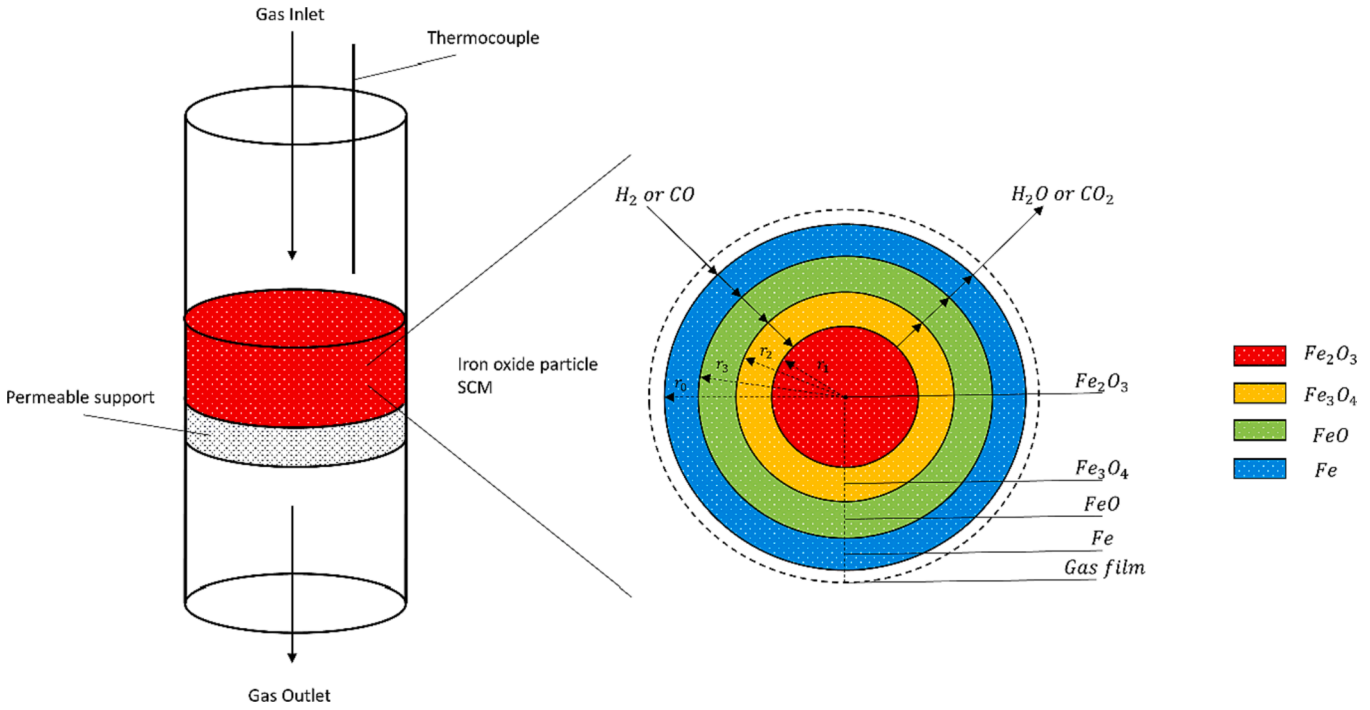

Fig. 2. Fixed bed reactor scheme and three-interface shrinking core model, with SCM transient reduction of hematite particle.

where X_j represents the degree of *j*:th reaction front (Fe_2O_3 reduction, etc.), $n_0 = 3m_0/M_{Fe_2O_3}$ is the initial oxygen content calculated from the initial mass, m_0,

$$r_j(t,z) = \frac{P}{RT}\frac{3}{r_0}\frac{1}{A_j(t,z)\big|_f}\left(\frac{N_j(t,z)\big|_f}{W(t,z)\big|_f} - y_{\mathrm{H_2},j,\mathrm{eq}}(t,z)\right) \tag{2}$$

where R is the gas constant, r_0 is the radius of the initial particle, $y_{\mathrm{H_2},j,\mathrm{eq}}$ is the equilibrium molar fraction of H_2 for the *j*:th reaction, while P and T are the operating pressure and temperature, respectively. $y_{\mathrm{H_2},j,\mathrm{eq}}$ is calculated for each reaction front according to

$$y_{i,j,\mathrm{eq}}(t,z) = \frac{1}{1+K_j}\cdot\left(y_{\mathrm{H_2},j}(t,z) + y_{\mathrm{H_2O},j}(t,z)\right) \tag{3}$$

where $y_{\mathrm{H_2},j}$ and $y_{\mathrm{H_2O},j}$ represent the molar fractions of the gaseous reactant and product at a given reaction front (also taking into account the presence of inert gas), while K_j is the equilibrium constant of the *j*:th reaction.

Starting from the reduction of hematite, the reactive network moves from an initial phase, in which all three reaction fronts are accessible, to the next phase after the complete reduction of hematite ($X_1(t,z) = 1$) in which only two fronts are present. Similarly, when the magnetite is completely reduced ($X_2(t,z) = 1$), there is a transition to a single-front system. In general, the formulations of the coefficients A_j, W_j, and N_j that define the reduction rate must necessarily change as a function of the number of possible reductions ($A_j(t,z)\big|_f$, $W_j(t,z)\big|_f$ and $N_j(t,z)\big|_f$). The value of the parameter f, which is defined in the system of equations (4), indicates the number of reaction fronts at the time f and the axial coordinate z

$$\text{if}\begin{cases} X_1(t,z) < 1 & f=3 \quad j=1,2,3 \\ X_1(t,z) = 1 \wedge X_2(t,z) < 1 & f=2 \quad j=2,3 \\ X_1(t,z) = 1 \wedge X_2(t,z) = 1 \wedge X_3(t,z) < 1 & f=1 \quad j=3 \end{cases} \tag{4}$$

N_j represents the effective reduction contribution of each reaction, while W is the total resistance of the system. Both are defined starting from the terms that respectively identify the resistances of the process: kinetic A_j, intraparticle diffusion B_j, and external diffusion F. The equations derived for the case of a triple reaction front ($f = 3$) are

$$\begin{aligned} N_1(t,z)\big|_3 = {} & (A_1A_2A_3)\cdot y_{\mathrm{H_2},1} + [A_1A_2(B_3+F)]\cdot y_{\mathrm{H_2},3,\mathrm{eq}} + [A_1A_3B_2 + A_1A_3(B_3 \\ & + F) + A_1B_2(B_3+F)]\cdot y_{\mathrm{H_2},2,\mathrm{eq}} + [A_3B_1(A_2+B_2) + A_3B_1(A_2 \\ & + B_2) + B_1(A_2+B_2)(B_3+F) + A_2A_3B_2 + A_2A_3(B_3 \\ & + F) + A_2B_2(B_3+F)]\cdot y_{\mathrm{H_2},1,\mathrm{eq}} \end{aligned} \tag{5}$$

$$\begin{aligned} N_2(t,z)\big|_3 = {} & [A_2A_3(A_1+B_1)]\cdot y_{\mathrm{H_2},2} + [A_2(A_1+B_1)(B_3+F)]\cdot y_{\mathrm{H_2},3,\mathrm{eq}} + [A_3(A_1 \\ & + B_1)(B_3+F) + B_2(A_1+B_1)(B_3+F) + A_3B_2(A_1 \\ & + B_1)]\cdot y_{\mathrm{H_2},2,\mathrm{eq}} + [A_2A_3B_2 + A_2A_3B_2 + A_2B_2(B_3+F) + A_2A_3(B_3 \\ & + F)]\cdot y_{\mathrm{H_2},1,\mathrm{eq}} \end{aligned} \tag{6}$$

$$\begin{aligned} N_3(t,z)\big|_3 = {} & [A_3(A_1+B_1)(A_2+B_2) + A_2A_3B_2]\cdot y_{\mathrm{H_2},3} + [(A_1+B_1)(A_2 \\ & + B_2)(B_3+F) + A_2B_2(B_3+F)]\cdot y_{\mathrm{H_2},3,\mathrm{eq}} + [A_3(A_1+B_1)(B_3 \\ & + F)]\cdot y_{\mathrm{H_2},2,eq} + [A_2A_3(B_3+F)]\cdot y_{\mathrm{H_2},1,\mathrm{eq}} \end{aligned} \tag{7}$$

$$\begin{aligned} W(t,z)\big|_3 = {} & \{(A_1+B_1)\cdot[A_3(A_2+B_2+B_3+F) + (A_2+B_2)\cdot(B_3+F)] \\ & + A_2[A_3(B_2+B_3+F) + B_2(B_3+F)]\}\cdot y_{H_2,1,eq} \end{aligned} \tag{8}$$

The corresponding equations for calculating the contributions in the case of a double reaction front ($f = 2$) are

$$\begin{aligned} N_2(t,z)\big|_2 = {} & (A_2A_3)\cdot y_{\mathrm{H_2},2} + [A_2(B_3+F)]\cdot y_{\mathrm{H_2},3,\mathrm{eq}} + [A_2B_1 + (A_3+B_2)(B_3 \\ & + F)]\cdot y_{\mathrm{H_2},2,\mathrm{eq}} \end{aligned} \tag{9}$$

$$\begin{aligned} N_3(t,z)\big|_2 = {} & A_3(A_2+B_2)\cdot y_{\mathrm{H_2},2} + [(A_2+B_2)(B_3+F)]\cdot y_{\mathrm{H_2},3,\mathrm{eq}} + [A_3(B_3 \\ & + F)]\cdot y_{\mathrm{H_2},2,\mathrm{eq}} \end{aligned} \tag{10}$$

$$W(t,z)\big|_2 = A_3(A_2+B_2+B_3+F) + (A_2+B_2)\cdot(B_3+F) \tag{11}$$

while the system for the case of a single reaction front ($f = 1$) is

$$N_3(t,z)\,|_1 = y_{H_2,3}(t,z) - y_{H_2,3,eq}(t,z) \tag{12}$$

$$W(t,z)\,|_1 = \frac{A_3 + B_3 + F}{A_3} \tag{13}$$

This modeling approach proves particularly useful because it also allows for evaluation of the potential reduction of the other two iron oxides. The evaluations of the A_j, B_j and F terms are

$$A_j(t,z)\,\big|_f = \frac{1}{\left(1 - X_j(t,z)\right)^{\frac{2}{3}}} \cdot \frac{1}{k_j \cdot \left(1 + \frac{1}{K_j}\right)} \tag{14}$$

$$B_j(t,z)\,\big|_f = \frac{\left(1 - X_{j+1}(t,z)\right)^{\frac{1}{3}} - \left(1 - X_j(t,z)\right)^{\frac{1}{3}}}{\left(1 - X_j(t,z)\right)^{\frac{1}{3}} \cdot \left(1 - X_{j+1}(t,z)\right)^{\frac{1}{3}}} \cdot \frac{r_0}{D_j} \tag{15}$$

$$F = \frac{1}{H} \tag{16}$$

where k_j is the kinetic constant of the j:th reaction front, D_j is the intraparticle diffusion coefficient, which depends on the morphological properties of the oxide, while H is the external diffusion coefficient. As for the external diffusion phenomena, the resistance to the transport of gases outside the particles is negligible in the present case because the packed bed consists of iron oxide fines ($r_0 < 5\mu$m), so H is very high. The kinetic (Chu et al. 2005), thermodynamic (Zhang et al., 2013), and diffusion (Takahashi et al., 1971) parameters used in the model are calculated using values reported in the literature, based on the formulas (cf. Tables 2 and 3)

$$k_j = k_{j,\mathrm{ref}} \cdot \exp\left[\left(-\frac{E_{a,j}}{R}\right) \cdot \left(\frac{1}{T} - \frac{1}{T_{\mathrm{ref}}}\right)\right] \tag{17}$$

$$K_j = \exp\left(-\frac{\Delta G_j}{RT}\right) = \exp\left(-\frac{\Delta H_j - T\Delta S_j}{RT}\right) \tag{18}$$

$$D_j = d_{1,j} \cdot \exp\left(d_{2,j} - \frac{d_{3,j}}{T}\right) \tag{19}$$

In the equations, $k_{j,\mathrm{ref}}$ and $E_{a,j}$ are the pre-exponential factor and activation energy, respectively, of the j:th reduction used in the modified Arrhenius equation, T_{ref} is the reference temperature (here 600 °C), ΔH_j and ΔS_j represent the enthalpy and entropy changes of the reaction by which the Gibbs free energy changes (ΔG_j) can be determined, while the terms $d_{1,j}$, $d_{2,j}$ and $d_{3,j}$ are coefficients of the empirical equation describing intraparticle diffusion. The intrinsic properties of the solid (e.g. porosity), which are considered constant under the assumptions of the shrinking core model, are implicitly expressed in the $d_{1,j}$, $d_{2,j}$ and $d_{3,j}$ coefficients. The diffusion of gaseous species in the solid is therefore mechanistically described as a molecular diffusion phenomenon.

Table 2
Fixed model parameters.

Parameter	Value	Unit	Parameter	Value	Unit
$d_{1,1}$*	$1\cdot10^{-4}$	$m^2 s^{-1}$	$g_{1,2}$**	$7\cdot10^{5}$	$W m^{-1} K^{-1}$
$d_{2,1}$*	3.43	–	$g_{2,2}$**	1.1	–
$d_{3,1}$*	$4.2\cdot10^{3}$	K	$g_{3,2}$**	$8.5\cdot10^{2}$	–
$d_{1,2}$*	$1\cdot10^{-4}$	$m^2 s^{-1}$	$g_{4,2}$**	$-1.5\cdot10^{5}$	–
$d_{2,2}$*	5.64	–	$g_{1,3}$**	3.7	$W m^{-1} K^{-1}$
$d_{2,3}$*	$6.8\cdot10^{3}$	K	$g_{2,3}$**	$-3.8\cdot10^{-1}$	–
$d_{1,3}$*	$1\cdot10^{-4}$	$m^2 s^{-1}$	$g_{3,3}$**	$9.6\cdot10^{2}$	–
$d_{2,3}$*	4.77	–	$g_{4,3}$**	$1.9\cdot10^{6}$	–
$d_{3,3}$*	$5.9\cdot10^{3}$	K	$E_{a,1}$***	$33.4\cdot10^{3}$	$J mol^{-1}$
$g_{1,1}$**	$2.6\cdot10^{-3}$	$W m^{-1} K^{-1}$	$E_{a,2}$***	$58.2\cdot10^{3}$	$J mol^{-1}$
$g_{2,1}$**	$7.4\cdot10^{-1}$	–	$E_{a,3}$***	$57.1\cdot10^{3}$	$J mol^{-1}$
$g_{3,1}$**	9.0	–	ε	0.25	–
$g_{4,1}$**	0	–			

*(Takahashi et al., 1971).
**(CHEMCAD).
***(Chu et al., 2005).

Table 3
Key coefficients of model used for parametric analysis.

Parameter	Value	Unit
T	873	K
$k_{1,\mathrm{ref}}$*	$5\cdot10^{-5}$	$m s^{-1}$
$k_{2,\mathrm{ref}}$*	$2\cdot10^{-4}$	$m s^{-1}$
$k_{3,\mathrm{ref}}$*	$4\cdot10^{-5}$	$m s^{-1}$
D_z	$1\cdot10^{-6}$	$m^2 s^{-1}$
r_0	$2.5\cdot10^{-6}$	m
m_0	0.1	g
y_{H_2}	0.2	–
Q	20	$ml min^{-1}$

*(Chu et al., 2005).

2.3. Gas mass balance

Mass balance equations for H_2 and H_2O were formulated to describe the variation of reducing gas composition in the fixed bed by describing the interaction with the solid through the SCM

$$\frac{\partial c_i(t,z)}{\partial t} = \underbrace{-\frac{u}{h}\cdot\frac{\partial c_i(t,z)}{\partial z}}_{\text{Convection}} + \underbrace{\frac{D_z}{h^2}\cdot\frac{\partial^2 c_i(t,z)}{\partial z^2}}_{\text{Axial dispersion}} + \underbrace{\frac{1}{\varepsilon}\cdot\sum_{j|_f}^{3}\nu_{i,j}\cdot r_j(t,z)}_{\text{Reaction SCM}} \tag{20}$$

In the equation, c_i represents the concentration of the i:th species in the system, h is the fixed-bed height, u is the superficial gas velocity defined as the ratio between the volumetric flow rate of the gas and the (empty) cross-sectional area of the reactor, while D_z represents the coefficient of axial dispersion. $\nu_{i,j}$ is the stoichiometric coefficient of gaseous species i in reaction j (Table 1), while ε is the voidage of the bed.

The boundary conditions of the system of partial differential equations were defined at the reactor inlet ($z = 0$) and outlet ($z = 1$) as

$$c_i(t,z)\,|_{z=0} = c_{i,\mathrm{in}} \qquad \left.\frac{\partial c_i(t,z)}{\partial z}\right|_{z=1} = 0 \tag{21}$$

In this modeling work, the energy balance of the reduction of iron oxides with H_2 was not considered, although, as indicated in Table 1, the reactive network is endothermic overall. The reason for this exclusion lies in the operating conditions of the model, which describes the reduction of small beds of very fine ore particles, where the temperature gradients can be considered negligible, and an external controlled heat source guarantees that the temperature stays constant. In order to theoretically evaluate this assumption, the criterion

$$T_j^{\mathrm{center}} - T_j^{\mathrm{surface}} = \frac{D_j \cdot \left(-\Delta H_j\right)}{\lambda_j} \cdot \left(c_{H_2}^{\mathrm{surface}} - c_{H_2}^{\mathrm{center}}\right) \tag{22}$$

was used, where λ_j represents the thermal conductivity coefficient of the reacting oxides (Akiyamah et al., 1992). While the first term on the right-hand side is always less than 1 K m^3 mol^{-1} for all solids involved (in a range of $5\cdot10^{-2}$ – $1\cdot10^{-1}$ K m^3 mol^{-1}), the evaluation of the second term on the right-hand side can be done using as an example the worst-case scenario in terms of concentration variations between the surface and the center of the particle. This is represented by the maximum H_2 concentration in the absence of inert at 873 K ($c_{H_2}^{\mathrm{feed}} \approx 14$ mol m^{-3}) assumed as the surface composition and no H_2 in the core. An intra-particle temperature variation of $-6.49\cdot10^{-1}$ K, 1.61 K and 1.23 K is observed for the reduction of hematite, magnetite and wustite,

respectively. This result supports the assumption of a negligible intra-particle temperature variation, which is also supported by recent experimental findings by Hessling et al. (2022) that indicate temperature differences of less than 10 K between the surface and core of much larger (12 mm) pellet particles.

2.4. Local sensitivity analysis

Sensitivity analysis of a mathematical model can provide important preliminary information for future estimation of, for example, kinetics coefficients by evaluating the response of the model to parametric perturbations. For this purpose, a local sensitivity analysis was undertaken (Morris, 1991; Norton, 2015), calculating a sensitivity index

$$SSE_{m,\Delta} = \sqrt{\frac{1}{t_v \cdot z_v}\sum_{\chi=1}^{5}\sum_{l=1}^{z_v}\sum_{s=1}^{t_v}\left(\frac{C^{\chi}_{s,l}(p_1,\cdots,p_m \pm \Delta,\cdots,p_n) - C^{\chi}_{s,l}(p_1,\cdots,p_n)}{C^{\chi}_{s,l}(p_1,\cdots,p_n)\,|_{\max} - C^{\chi}_{s,l}(p_1,\cdots,p_n)\,|_{\min}}\right)^2} \tag{23}$$

after varying each parameter of interest individually by ±10 % or ±50 %. The sensitivity index expresses the standardized elemental effect of parameter $p_m(\pm\Delta)$ over the number n of parameters studied in the analysis (i.e., $k_{j,\mathrm{ref}}$, D_z, r_o, m_{O}, $y_{\mathrm{H_2}}$ and Q) calculated for all state variables $C^{\chi}_{s,l}$ considered (here gas composition and reduction degrees, i.e., 5) with respect to the values of the state variables calculated starting from chosen values of the p vector (i.e., the base case). The sensitivity is performed by comparing all values of the state variables in time and space of the system (indices s and l, respectively), where z_v represents the number of grid points of the dimensionless axial coordinate of the reactor while t_v is the number of simulated time points. The maximum and minimum values of the state variables used in the denominator of the index are set in relation to the overall reaction time. The sensitivity index is obtained divided the comparison by the number of samples per observed output.

2.5. Front reaction control

By definition, the kinetic terms describing the chemical reactions in the SCM do not depend on the amount of species in the solid phase, but exclusively on the compounds in the gas phase. For this reason, for certain combinations of the model parameters it is possible that an outer front in the SCM would move faster than an inner one, leading to physically infeasible states if the interfaces cross. To avoid this problem for both the local sensitivity study and future kinetic parameter estimation, a reaction front control procedure was developed. After calculating the value of $dX_j(t,z)/dt$ for time t, the future value $dX_j(t+\Delta t,z)/dt$ is estimated through the trapezoidal method, where Δt is defined as the maximum integration step of the solver of the model (cf. Section 2.6). If the new intermediate degree of reduction ($j > 1$ at $t + \Delta t$) is greater than that of the previous reaction, the equality of the derivatives over time in t are forced. Physically, this means that it is impossible for an outer front to cross an inner one, and at most it they can move with an equal rate. The key condition for controlling the front is

$$X_j(t+\Delta t,z) = X_{j+1}(t+\Delta t,z) \quad \text{if} \quad X_{j-1}(t+\Delta t,z) < X_j(t+\Delta t,z) \tag{24}$$

2.6. Numerical solution

The mathematical model was developed in Matlab 2023a by solving the system of partial differential equations, using the finite difference method (backward with respect to the first-order derivative of the space and centered with respect to the second-order derivative of the space), setting 50 grid points for the axial dimensionless coordinate of the reactor. The ordinary differential equations are solved using the ode15s function, a variable step size, variable order solver based on numerical differentiation formulas of 1–5 orders. This, together with the front reaction control, was found to yield robust solutions for practically arbitrary parameter values in the model.

2.7. Experimental setup

Reduction experiments were performed with an Autochem2910, which is generally used for chemosorption studies on catalysts. This experimental apparatus made it possible to undertake iron oxide reduction in a fixed bed configuration by feeding the hydrogen-containing gas from above. The oxide fines charged into the glass reactor are retained by a porous support, which also allows the effluent gases to reach the Thermal Conductivity Detector (TCD) for compositional analysis. The reagent bed (diameter 8 mm) consists of hematite powder (purity 97 %, Sigma Aldrich) with a particle diameter of less than 5 μm (cf. Fig. 2). The probing experiments were performed isothermally with pre-determined H_2/Ar molar ratio (H_2, 99.9 % purity; Ar, 99.9 % purity) and total gas flow rate. The signal obtained from the TCD is a function of the composition of the gas mixture leaving the reactor and the thermal conductivity of the chemical species involved. Since the thermal conductivity of H_2 is much higher than that of H_2O and Ar (which are very similar), the TCD signal roughly reflects the share of hydrogen in the gas leaving the reactive system. As an example, Fig. 3 shows experimental results of the reduction of a bed of 0.1 g of fine hematite (bed diameter of 8.5 mm and bed height of approximately 0.5 mm), carried out at different temperatures but at the same gas volume flow rate (20 mL/min) and molar ratio (H_2:Ar = 1:4), where the normalized signal of TCD is plotted over time. The normalization was done by dividing the TCD value of the outgoing gas by that of the incoming gas.

The signals show very different trends and changes in slope, which clearly depend on the number of reactions involved and their rate as the temperature changes. In general, the reaction can be said to be complete when the signal stabilizes at a value of 1, which means that no H_2 is consumed in the bed. The reduction at 773 K should not proceed via the FeO intermediate (cf. Fig. 1), which justifies its simpler form compared to the other two cases, while the form of the signal obtained at 1073 K appears to be an accelerated version of the reaction at 873 K. To better understand the observed phenomenological dynamics, a profound experimental study supported by a well-characterized mathematical model is required.

To simulate the TCD signal, equations were introduced into the mathematical model that depend on the operating temperature and serve to evaluate the contribution of the thermal conductivity of the gases involved in the chemical reaction. The relationships and parameters ($g_{1,i}, g_{2,i}, g_{3,i}$ and $g_{4,i}$) were taken from CHEMCAD.

$$\lambda_i = \frac{g_{1,i}\cdot(T/\mathrm{K})^{g_{2,i}}}{1 + \frac{g_{3,i}}{(T/\mathrm{K})} + \frac{g_{4,i}}{(T/\mathrm{K})^2}} \tag{25}$$

3. Numerical results

3.1. Model simulation

A parametric study was conducted on the mathematical model describing the bed reduction of fine iron oxides particles in an isothermal fixed bed described through the theoretical assumptions of the three-interface SCM to evaluate its performance.

The study was commenced by utilizing thermodynamic and kinetic parameters reported in the literature, carefully selecting the operating conditions (T, Q, $c_{\mathrm{H_2,in}}$, etc.) and the other structural coefficients of the model (D_z, ε, etc.). Table 2 and Table 3 list the values and units of all fixed parameters or key coefficients; the latter represent the base case values and form the starting point for the parametric analysis of the mathematical model.

Given the wide variation in the activation energy found in the

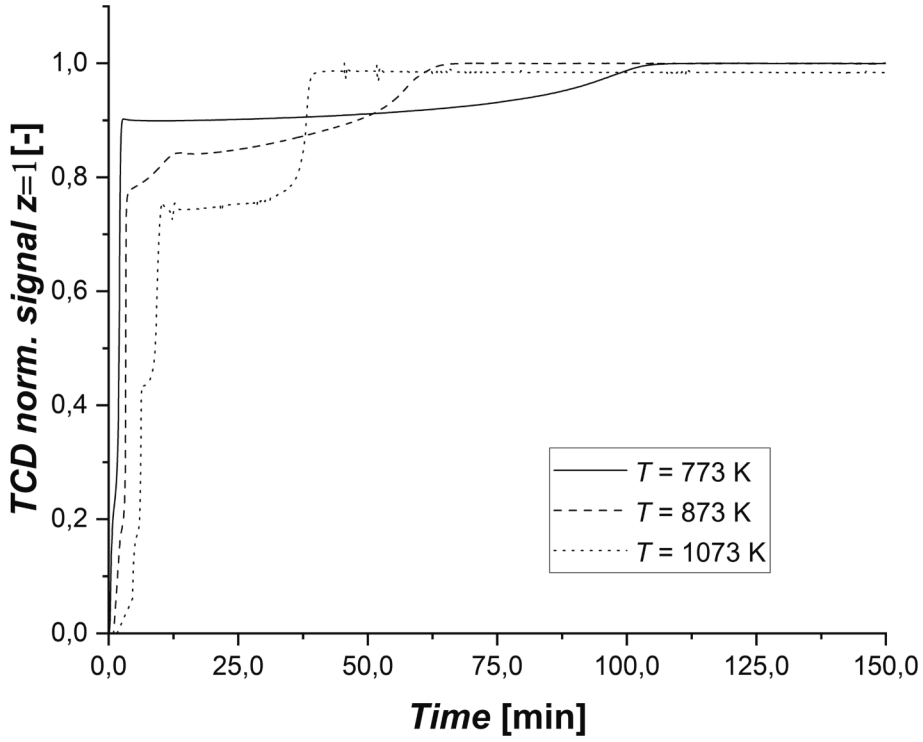

Fig. 3. Examples of experimental results relating to the reduction of hematite powder in a fixed bed reactor at different operating temperatures.

literature for each reduction, the kinetic parameters used in the model were chosen so that the different $E_{a,j}$ represent an average of those reported in the literature accompanied by the reference kinetic constants.

Figs. 4 and 5 show the main results of the model simulating the reduction of a 0.1 g (pure) hematite bed at a temperature of 873 K, a total gas volume flow of 20 mL/min, and a feed molar ratio of H_2:Ar of 1:4 using the base case set of parameters, reported in Table 3.

The contour plots in Fig. 4 show the axial profiles of the mole fractions of (a) hematite, (b) magnetite, (c), wüstite and (d) iron as a function of reactor axial coordinate and reaction time. The hematite converts completely in less than 5 min, promoting the rapid production of the first intermediate. In Fig. 4b, the balance between the production and consumption of magnetite is peculiar when focusing on the difference between reactor inlet and outlet. In the beginning ($t < 5$min), the formation of magnetite agrees with the consumption of the initial reactant and reaches mole fractions of about 0.5 throughout the reactor. However, near the reactor inlet ($z = 0$), magnetite is completely consumed within the first 5 min, promoting the formation of the second intermediate (wüstite). This is due to the constant supply of fresh hydrogen at the reactor inlet, which strongly drives the formation of products in all reactions (see also Fig. 5a). For this reason in the upper part of the bed, the amount water produced during the reduction is always lower than the amount of H_2, so the reaction rates are not limited by equilibrium constraints. Approaching the lower end of the reactor, the dynamics of the system change radically, leading to a significant accumulation of magnetite (with a molar ratio approaching unity) in the first 10 min. The consumption of Fe_3O_4 in the lower bed is significantly slowed down by the high consumption of H_2 and the associated production of H_2O in the upper parts of the bed. The accumulation of water in the gas phase, which is increased by the resistance to inter- and intraparticle transport, thermodynamically slows down the chemical reaction. This results in a limited driving force for the reaction, so approximately 25 min is required to complete the reduction of the magnetite in the whole bed. As seen in Fig. 4c, a similar trend is observed for wüstite in the lower region of the bed: while complete reduction is observed at the top of the bed in about 30 min, it takes about 90 min to fully convert the wüstite to metallic iron. The reaction of FeO to Fe is also kinetically the slowest among the reduction steps (Spreitzer & Schenk, 2019). The simulation results underline a very important aspect, also for the definition of a set of experimental tests, namely the need to consider the quite complex impact of the bed dynamics on the total reduction time.

Figure 5a and b show the mole fractions of H_2 and H_2O in the gas phase as a function of axial coordinate and time. The molar ratio of hydrogen in the system is always high (0.2) at the reactor entrance, but only for the initial phase of the experiment it is almost halved at the reactor end, confirming the observations of the solid phase composition plots in Fig. 4. Water naturally exhibits a mirror image pattern to hydrogen. Fig. 5c shows the temporal development of the mole fractions of the solid species in the entire reactor, indicating the time intervals at which the disappearance of some reaction intermediates can be observed. Fig. 5d shows an example of a normalized TCD signal calculated based on the simulated composition of the reactor off-gas (H_2, H_2O, and Ar), as the sum of the mole fractions multiplied by the corresponding thermal conductivity coefficients obtained by empirical equations (24). This signal provides important information about the course of the chemical reactions, which end when the value of one is reached (which implies that the off-gas has identical composition as the feed gas). The different slopes of the TCD curve reflect the three stages of the reduction, indicating when one reaction ends and the next becomes the dominant one. Comparison between Fig. 5c and 5d confirms that the disappearance of an intermediate oxide corresponds to a particular change in the slope of the simulated signal. In this way, it is possible both to evaluate the different modeling results of the parametric study by directly comparing the simulated signals and to perform a first analysis of the quality of the model compared to the experimental data.

3.2. *Parametric investigation*

Several simulations were performed to evaluate the model's response to the parametric perturbation in which a parameter or operating condition is perturbed from its base-point value (cf. Table 3). In this section

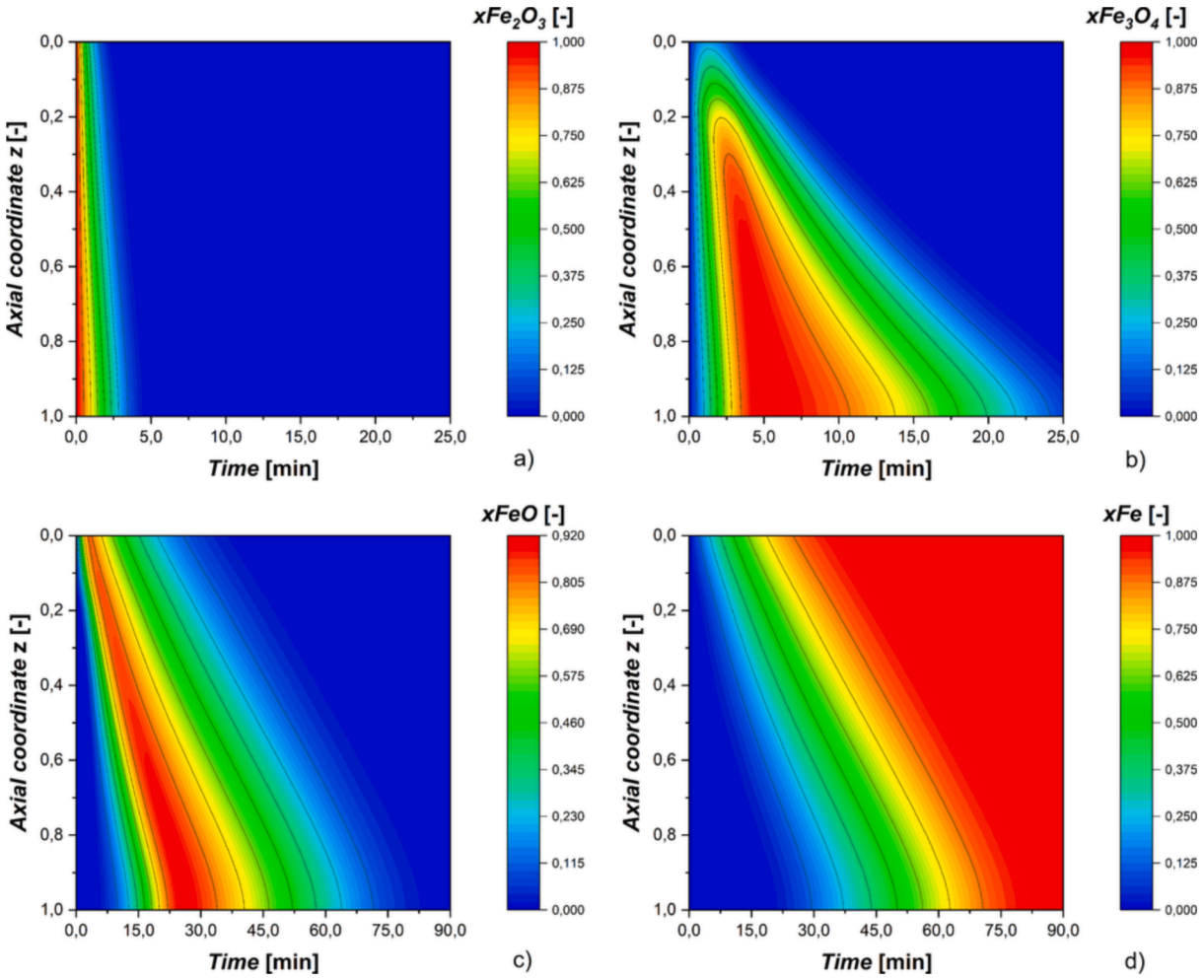

Fig. 4. Axial bed profiles over time of the iron and iron oxides: (a) Fe_2O_3, (b) Fe_3O_4, (c) FeO and (d) Fe, where the gas enters from above. Note the different time scales of the top and bottom panels.

we present some results of the effect of key parameters on the reduction behavior. The main purpose of this parametric study is to show how model parameters and boundary conditions affect the reduction of iron oxides. These results can be used to gain a comprehensive understanding of the system and how it would manifest in the TCD signal, which is the main information of the experimental device. This analysis is also useful for an upcoming parameter estimation where it is important to identify factors with significant effects.

3.3. Temperature

The operating temperature is one of the most important parameters of the model because it affects the intraparticle diffusion phenomena (Eq. 19) as well as the kinetics (Eq. 17) and thermodynamics (Eq. 18). It is well known that in reactions in gas/solid systems, both with heterogeneous catalysts and with reactive solids, the different dependence of diffusion and kinetic phenomena on temperature has a crucial influence on the limiting process, which is kinetics at low operative temperature and diffusion at high T. Fig. 6 shows the simulated TCD curves for the off-gas in the reduction of hematite at increasing operating temperatures.

As can be seen, the simulation results are qualitatively similar to those obtained in the experimental results illustrated in Fig. 3 under the same operating conditions. The temperature range of 873–1173 K is interesting since the formation of wüstite is suppressed below 843 K (Zhang et al., 2013), while most experimental results as reported in the literature are for temperatures lower than 1173 K (Spreitzer & Shenk, 2019). An increased temperature shortens the overall reaction time, and at 1173 K the total time that is less than half of the time required for complete reduction at 873 K. The simulated TCD signal in the first few minutes of the reaction decreases with increasing temperature due to the rapid H_2 consumption by the hematite and magnetite reductions. For temperatures below 1073 K, the slope changes of the curves which reflect the approach of complete reduction of the hematite are clearly observed, but they are less clear beyond this temperature as the rate of the magnetite-to-wüstite reaction increases. At high temperatures, the point of complete magnetite reduction becomes more evident, seen as a large change in the slope of the curve. The trend of the TCD signal becomes progressively flatter during the initial stage of the wüstite reduction, implying that at 1173 K the reaction consumes a constant amount of H_2 for almost 10 min. Due to the high presence of H_2O produced by the oxides in the upper parts of the bed, the driving force of the reaction in the lower parts of the bed is low and may vanish if the gas reaches equilibrium conditions.

3.4. Reference kinetic constants

The pre-exponential reference kinetic constants (cf. Eq. (17)) are among the most important parameters in the model, as they affect the kinetic resistance terms A_j (cf. Eq. (14)) and thus the reaction rates of the series of reduction steps. Fig. 7 shows the results of the effect of the first ($k_{1,\mathrm{ref}}$), second ($k_{2,\mathrm{ref}}$), and third ($k_{3,\mathrm{ref}}$) reference kinetic constants,

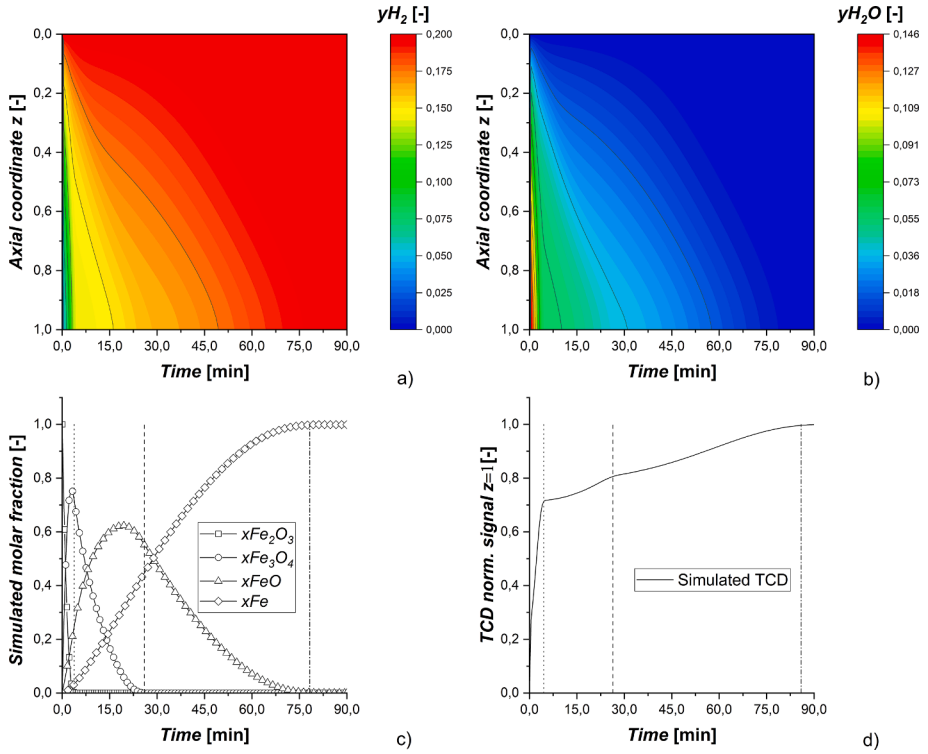

Fig. 5. Axial bed profiles over time of the gas phase: H_2 (a) and H_2O (b). Simulated TCD signal from off-gas composition (c). Dot line represents the end of the reduction of the major part of Fe_2O_3, dashed line the end of the reduction of the major part of Fe_3O_4, dot-dash line the end of the reduction.

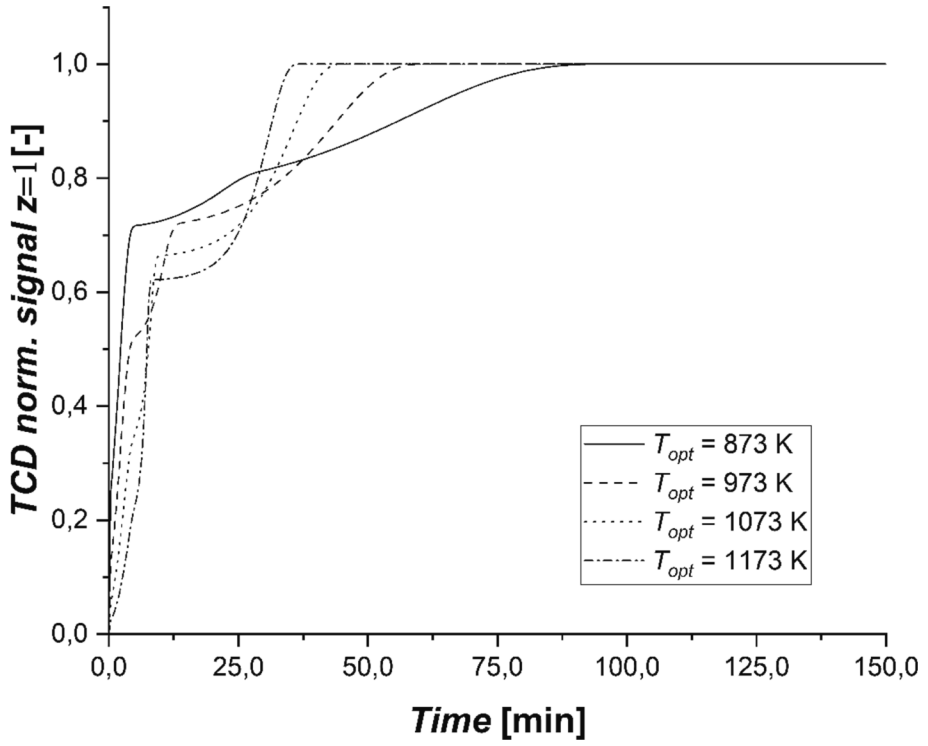

Fig. 6. Simulated TCD signals from off-gas composition over time, studying the effect of temperature.

respectively, on the simulated TCD signals of the gases leaving the reactor.

The variation of the first pre-exponential constant, $k_{1,ref}$, which is related to the reduction of hematite, mainly affects the initial phase of the reaction. Studying the variation of the parameter in an interval between $2.5{\cdot}10^{-5}$ m s^{-1} and $1.0{\cdot}10^{-4}$ m s^{-1}, it is possible to observe the increase of the kinetic parameter promotes the first reaction, as seen in Fig. 7a, but the effect on the overall reduction is minor, since the hematite-magnetite steps is the fastest one. When the parameter assumes the maximum value, the reaction is completed in less than 5 min,

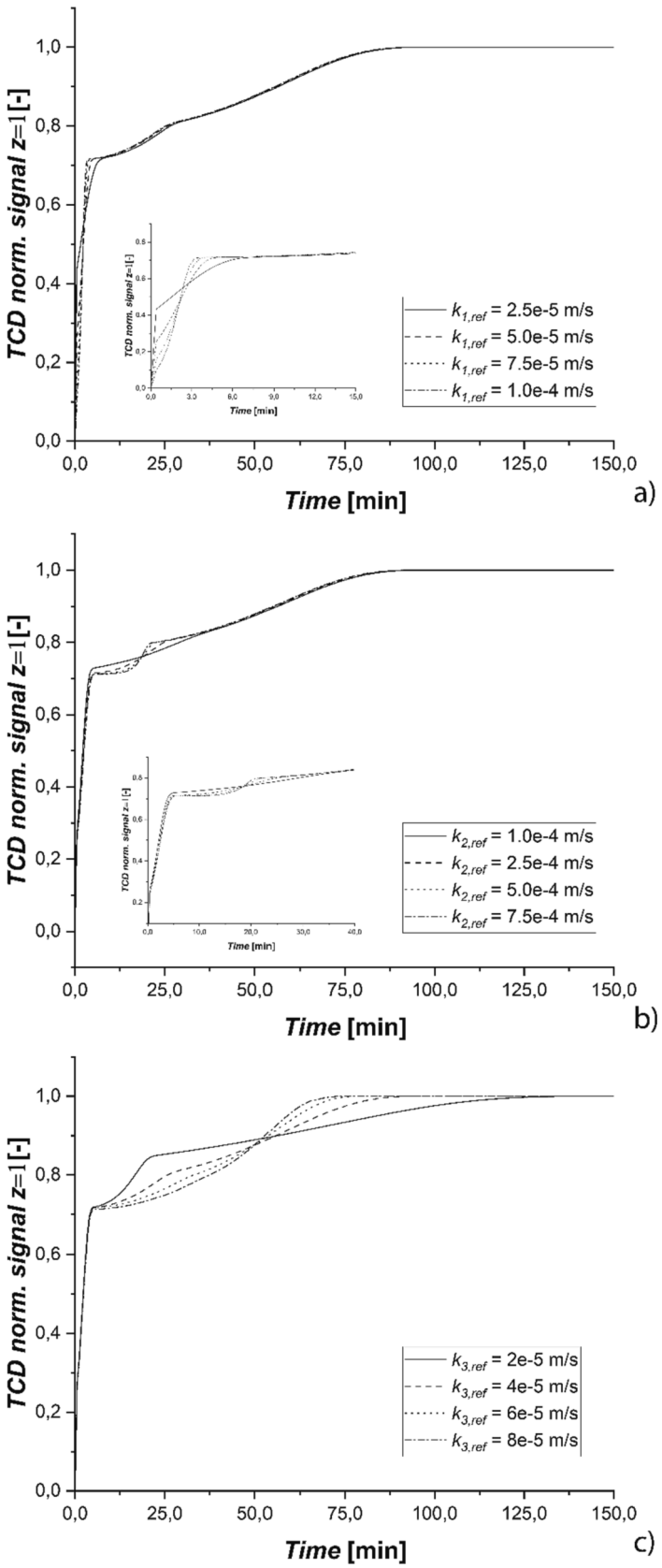

Fig. 7. Simulated TCD signals from off-gas composition over time, studying the effect of the reference kinetic constants: (a) $k_{1,\mathrm{ref}}$, (b) $k_{2,\mathrm{ref}}$ and (c) $k_{3,\mathrm{ref}}$.

which is half of the time needed to complete the first reduction step if the parameter assumes its minimum value.

The second pre-exponential kinetic constant, $k_{2,ref}$, affects mainly the TCD in the middle area of the figure and very little the part of the signal where the hematite reduction is completed. By increasing this parameter from $1.0{\cdot}10^{-4}$ m s^{-1} to $7.5{\cdot}10^{-4}$ m s^{-1}, the time of the magnetite-to-wüstite reaction step (Fe_3O_4) is reduced, although at high values the chemical reaction becomes thermodynamically limited due to the presence of H_2O produced in the first two reactions (yielding a plateau in the TCD signal). In contrast to the subsequent reactions, the reduction of hematite is never thermodynamically limited (cf. Fig. 1); this leads the system experiencing an initial phase where a water pulse propagates through the bed. If the value of $k_{2,ref}$ is decreased, the slopes become much less pronounced, and it is no longer possible to discern the end point of the second reaction in the TCD signal. At the smallest value of $k_{2,ref}$ studied, the magnetite reduction is so slow that its contribution to the TCD overlaps with that of the wüstite reduction.

As expected, the third pre-exponential kinetic constant, $k_{3,ref}$, related to wüstite reduction has the strongest influence on the model results, for both Fe_3O_4 and FeO reduction, being crucial in determining the overall reaction time. By manipulating the parameter in the range between $2{\cdot}10^{-5}$ m s^{-1} and $8{\cdot}10^{-5}$ m s^{-1}, it is noted that the as the value of the parameter decreases, the lower H_2 consumption in the bottom regions of the bed, where more wüstite is initially present, favors a rapid reduction of unreacted magnetite in the lower bed. This is seen as an increasingly pronounced peak in the signal due to the complete reduction of Fe_3O_4. Conversely, a high value of $k_{3,ref}$ makes the slope variation disappear, favoring greater water production and consequently leading to kinetic (i.e., low driving forces) and thermodynamic limitations. The overall reaction time changes significantly, varying from about 70 min for the maximum $k_{3,ref}$ value to 150 min for the minimum value.

3.5. Axial dispersion

The axial dispersion parameter D_z (cf. Eq. (20)) influences the gas-side mass balance through the resistance to interparticle transport thus affecting all reaction steps. Fig. 8 that depicts the results of perturbing the value of D_z between $1{\cdot}10^{-6}$ m^2s^{-1} and $5{\cdot}10^{-5}$ m^2s^{-1} shows that even a modest change in the parameter leads to large changes in the system. As the coefficient increases, the resistance to transport of the gaseous species through the reactor decreases, allowing them to cross the bed more efficiently, leading to enhanced reactions. For the same reason, the thermodynamic limitations due to the presence of water are also lesser as it is more easily removed from the bed. The overall reaction time is about 50 min for the maximum value of the parameter, while it is about 90 min for the minimum value of D_z.

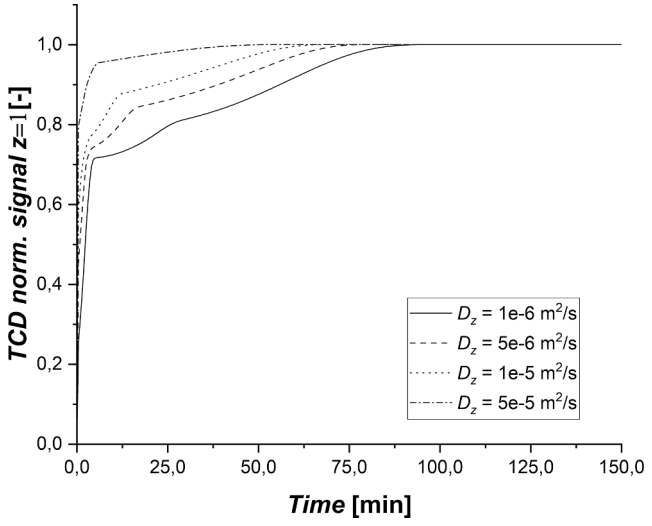

Fig. 8. Simulated TCD signals from off-gas composition over time, studying the effect of axial dispersion.

3.6. Particle radius

The particle radius influences the model decisively through the resistance to intraparticle transport (B_j) and the reaction rate, given the assumptions of the SCM. It also affects the surface area. Fig. 9 shows the results of varying the value of r_0 from 1 μm to 5 μm, indicating that the appearance of the TCD curve changes substantially with the particle radius. As the particle radius decreases, the internal diffusion resistance become less relevant and an important increase in the reaction rate is observed for all reduction steps due to a larger surface area-to-volume ratio. Such events, with different weight significantly shortens the overall reaction time. The particle size mainly affects the reduction rates of magnetite and wüstite, as the reduction of hematite is very fast. It can be observed that as the granulometry of the solid decreases, thermodynamic limitations become more evident (plateaus in the TCD signal), which are due to the high reaction rate and the accumulation of H_2O in the lower zones of the bed.

3.7. Bed mass

The initial mass, m_0, of the oxide to be reduced influences not only the amount of oxygen (n_0) to be removed but also the height of the fixed bed in the gas-side mass balances. Fig. 10, which depicts how m affects the simulated TCD signals, indicates that a 50 % increase in the bed mass prolongs the overall reduction time by about 30 %. The effect of the fixed bed height through the increase of the resistance of the convection and interparticle diffusion phenomena is less relevant due to the small bed heights studied.

3.8. Gas composition

The composition of the feed gas naturally represents one of the most important factors for the reactions. By increasing the molar ratio of hydrogen, y_{H_2}, in the feed gas, the reduction of the oxides can be enhanced, as seen in Fig. 11, where feed mole fractions from 10 % to 40 % (with Ar as the complement) were applied. All steps of the reaction proceed faster, reducing the overall reaction time, and thermodynamic limitations are no longer obvious, particularly not for the higher H_2:Ar molar ratio where the driving force of the system is sufficient at all parts of the bed.

3.9. Volumetric gas flow rate

Finally, the effect of total volumetric gas flow rate, Q, of the feed, which mainly influences the convection phenomena (u) defined in the gas-side mass balance of the mathematical mode (Eq. (20)) was varied from 10 mL/min to 40 mL/min. As seen in Fig. 12, a high Q value yields a faster reduction because the reactant is supplied more quickly into the reactor, preventing hydrogen starvation.

3.10. Local sensitivity analysis

A local sensitivity analysis of a model is a useful method for evaluating and summarizing its response to perturbations of parameter values from those of a base case simulation. More importantly, it is valuable for comparing the effects emanating from different parameters, which yields important information for a subsequent parameter estimation: parameters with minor influence can be excluded from the estimation phase, reducing the complexity of the numerical problem. Fig. 13 shows the sensitivity index of key parameters of the model estimated by Eq. (22) (cf. Section 2.4) at two different operating temperatures, 873 K and 1173 K.

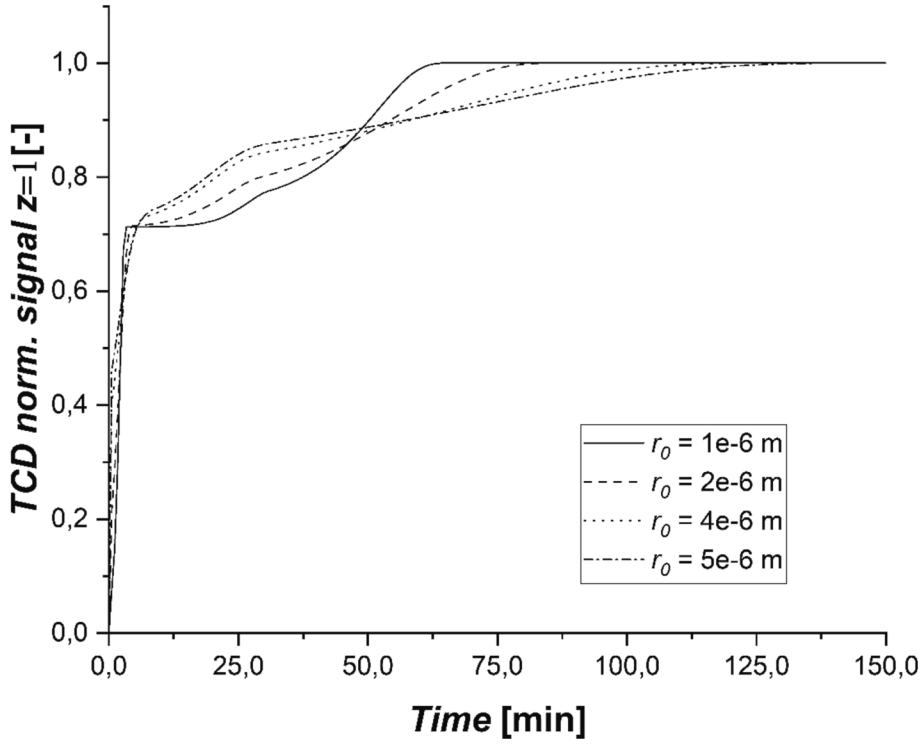

Fig. 9. Simulated TCD signals from off-gas composition over time, studying the effect of particle radius.

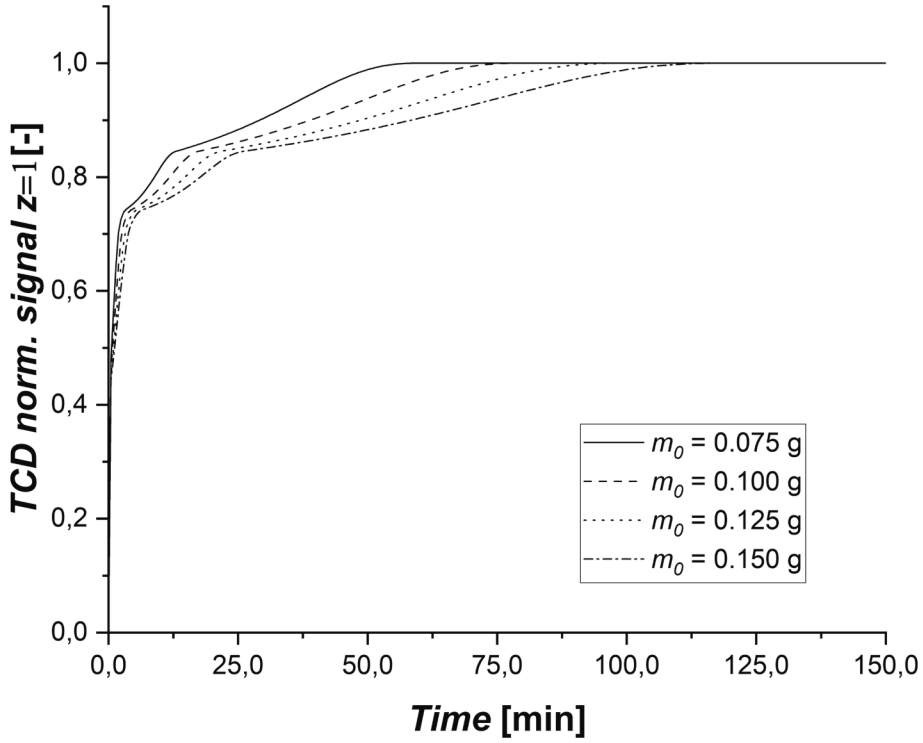

Fig. 10. Simulated TCD signals from off-gas composition over time, studying the effect of initial iron oxide mass.

Since many different phenomena described by the model depend on temperature, the local sensitivity analysis was performed by manipulating the model parameters at the different operating temperatures. Because of larger uncertainty, the pre-exponential constants were varied with respect to their base case values by ±50 % while all other parameters were perturbed by ±10 %. The graphs of the figure show that some coefficients, especially when increased, have a significant influence on the system behavior. In particular, $k_{3,ref}$, D_z and y_{H_2} have always the greatest impact and, in the case of the kinetic parameter, reach a sensitivity index ($SSE_{m,\Delta}$) of almost 70 % at 873 K. This result confirms what was already observed in the earlier analysis (cf. Fig. 6c), and that $k_{3,ref}$ also affects the rate of the magnetite-to-wüstite reaction. Increasing

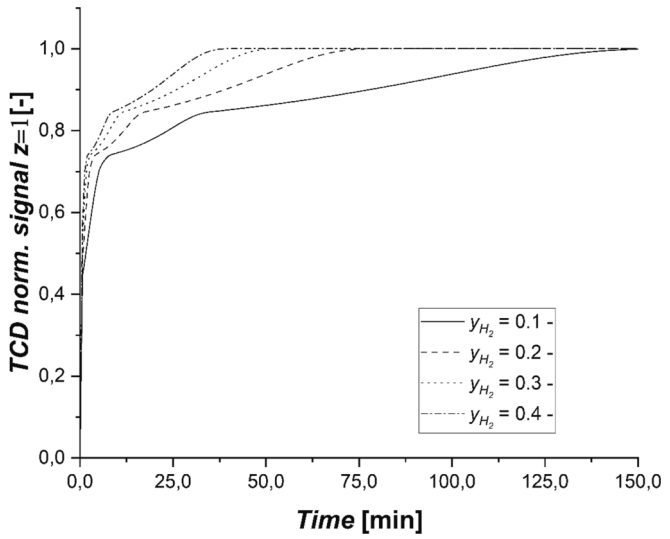

Fig. 11. Simulated TCD signals from off-gas composition over time, studying the effect of the molar ratio of hydrogen in the feed gas.

the values of D_z drastically accelerates the reduction in all steps, which stresses the need of an accurate expression for interparticle diffusion. A similar sensitivity is observed for y_{H_2} indicating the critical role played by the concentration of hydrogen in the gas. The remaining pre-exponential coefficients, together with the solid mass, form the set of parameters with medium influence on the model. The kinetic coefficients $k_{1,ref}$ and $k_{2,ref}$ have an effect mainly during the first 10–20 min of the reduction process which partially explains the lower impact of these parameters. Finally, r and Q have a smaller influence in the range of ±10 %. As for the role of temperature, the influence of changes in all the parameters tends to decrease with temperature due to the notable increase in reaction rates and the tendency to make diffusive phenomena more relevant.

3.11. Simulation and data comparison

In order to indicate the potential of the model to quantitatively explain the results of iron oxide reduction experiments undertaken (cf. Section 2.7), a preliminary attempt was made to mimic the conditions in a reduction experiment of a 0.1 g bed of fine hematite by a gas consisting of 20 % H_2 and 80 % Ar at a temperature of 873 K with a volumetric flow rate of the gas was $Q = 20\text{mL/min}$. After adjustments of the pre-exponential constants and the axial dispersion coefficient of the model to $k_{1,\text{ref}} = 6{\cdot}10^{-5}$, $k_{2,\text{ref}} = 5{\cdot}10^{-5}$, $k_{3,\text{ref}} = 2.4{\cdot}10^{-5}$ and $D_z = 3.9{\cdot}10^{-6}$, as shown in Fig. 14, the simulated TCD signal shows a good agreement with the experimentally observed counterpart. It should be pointed out that the activation energies were not changed from their base-point values because their influence on the system in the specific case is small as the operating temperature is equal to the reference temperature (T_{ref}) of the Arrhenius equation.

As can be seen, the model describes the experimental data well, including the changes in the slope of the signal reflecting the transition from one reduction step to the next. These encouraging results indicate the flexibility of the model and hold promise for a successful parameter estimation in forthcoming work using data from a large set of experiments. To this end, the ideal approach for the future is to conduct a large number of experiments in order to reduce experimental uncertainty and limit the number of parameters to be estimated to the most influential ones based on sensitivity analysis. Finally, because of the important role of the particle size, it will be necessary to further develop the mathematical model by considering the particle size distribution of the iron oxides fines.

4. Conclusions and future perspective

This work has presented a mathematical model of a system for reduction experiments of a small bed of iron oxide fines through which a hydrogen-containing gas passes at high temperature. A three-interface shrinking core model is used to describe the phenomena at and in the small particles, which is combined with a dynamic model of the particle

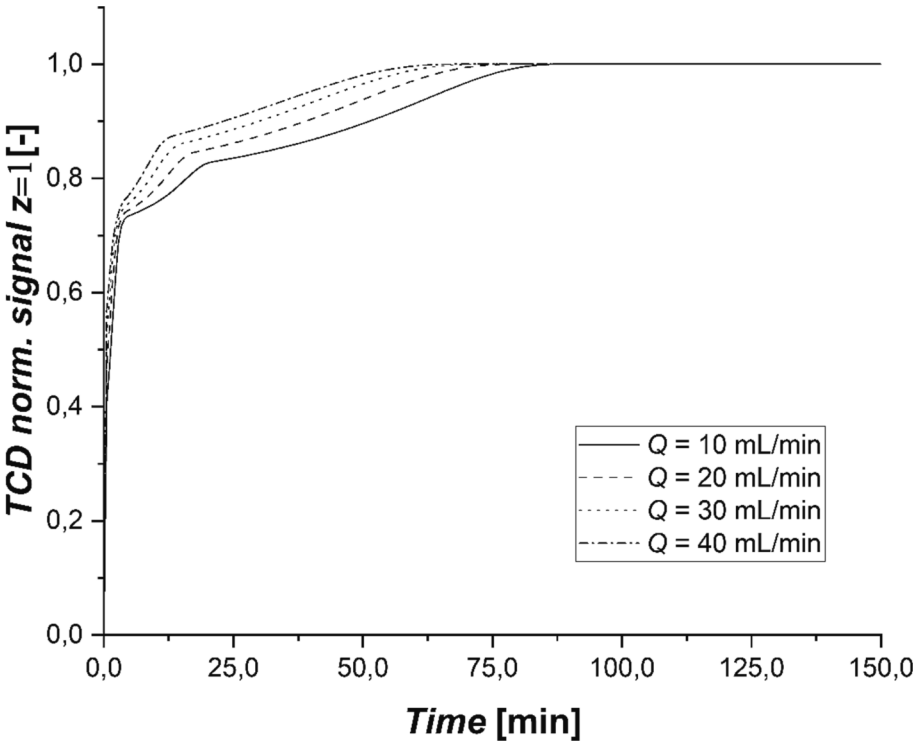

Fig. 12. Simulated TCD signals from off-gas composition over time, studying the effect of the gas flow rate.

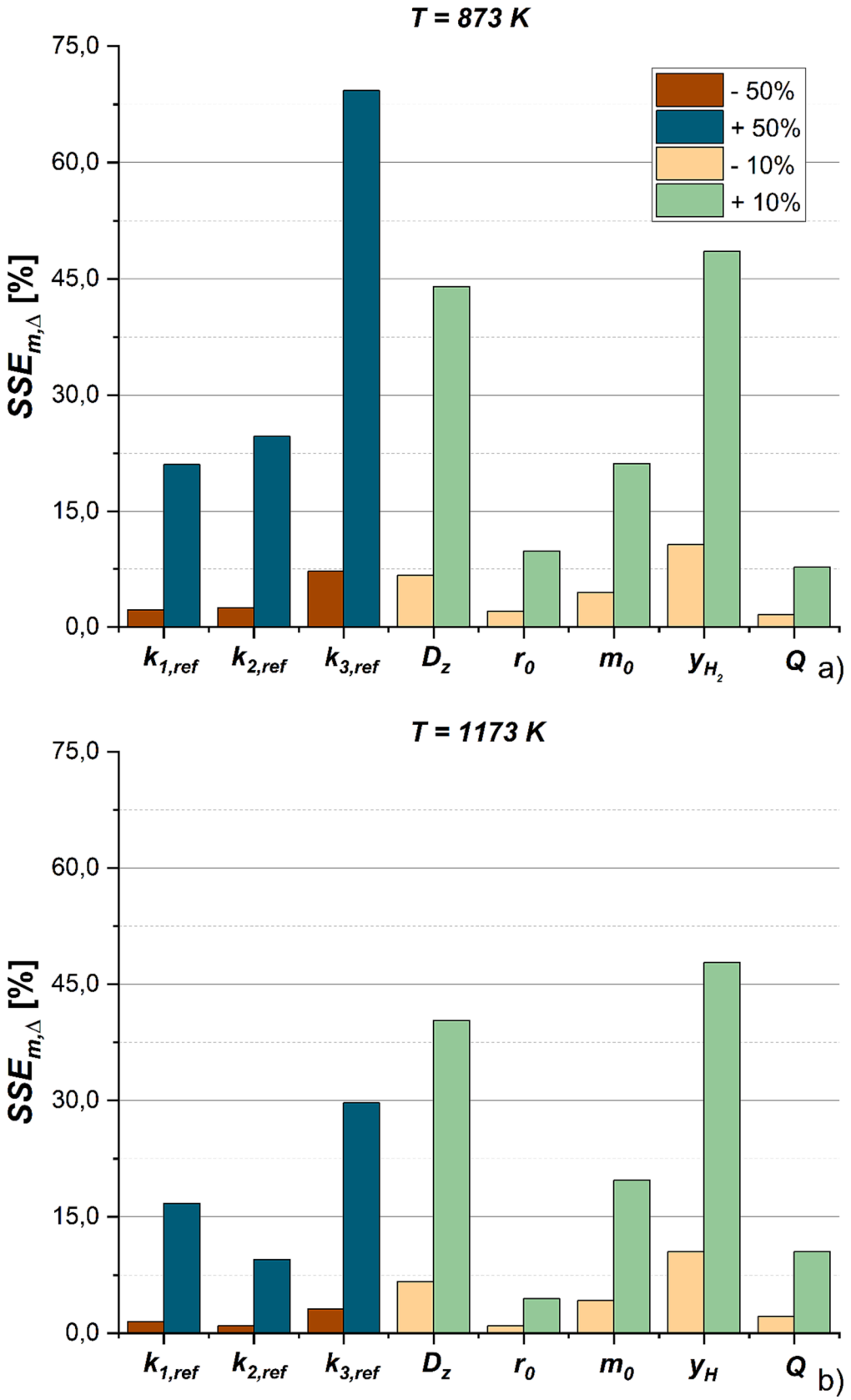

Fig. 13. Results of local sensitivity analysis: sensitivity index (cf. Eq. (22)) of key model parameters at (a) 873 K and (b) 1173 K.

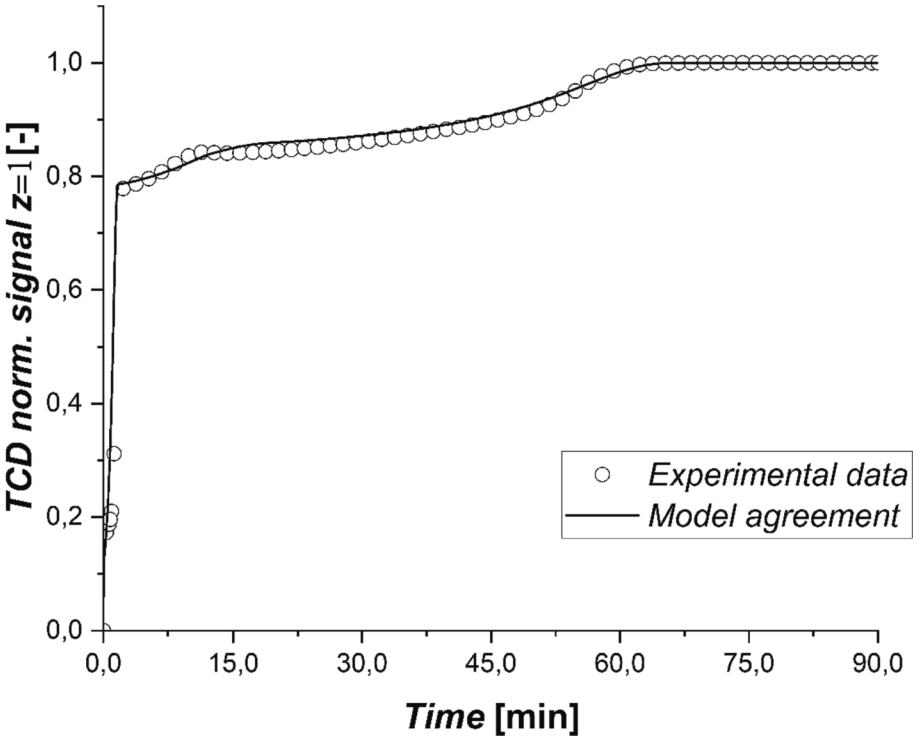

Fig. 14. Comparison between experimental data and simulation after adjustment of some model parameter values.

bed. Particular attention was paid to making the model robust so it can be executed for a wide range of model parameter values. With parameters of the kinetic and mass transfer expressions taken from the literature, the progress of the reduction reactions from hematite through magnetite and wüstite to metallic iron was simulated. A systematic analysis was undertaken to reveal the effect of different parameters and (boundary) conditions on the rate of the reduction steps. A comprehensive sensitivity study of the mathematical model was performed by analyzing its response to parametric perturbation, identifying parameters of particular importance. Finally, a preliminary attempt was made to reproduce experimental results by tuning a limited set of model parameters, and the model was demonstrated to have the flexibility to adapt to the results of the experiments quantified by the thermal conductivity of the gas leaving the bed. Based on a large set of data from systematic reduction experiments undertaken at different operating conditions, the kinetic parameters of each reaction step will be determined by the model in future work, comparing the findings with values reported in the literature. The experimental study has already been extended to analyzing the reduction kinetics of ground commercial ironmaking materials (BF and DR pellets) in the same fixed bed system. The findings will be used to evaluate the influence of the differences in the behaviour of morhphology and the chemical composition on the overall behavior. Moreover, the data will be used to update the kinetic expressions in simulation models of furnaces of industrial size developed by the group and its research partners (e.g., Shao et al., 2023, Mauret et al., 2023). This effort will mark the crucial initial stages of our research establishing a solid foundation for exploring the reduction of increasingly complex systems, which will include the study of the reduction of fines of commercial materials and eventually the scale-up of the model to consider solid particles of realistic size (e.g., pellets).

CRediT authorship contribution statement

Emiliano Salucci: Writing – original draft, Validation, Software, Methodology, Formal analysis. **Antonio D'Angelo:** Investigation, Data curation. **Vincenzo Russo:** Writing – review & editing, Supervision. **Henrik Grénman:** Writing – review & editing, Supervision, Project administration, Conceptualization. **Henrik Saxén:** Writing – review & editing, Supervision, Project administration, Conceptualization.

Declaration of competing interest

The authors declare that they have no known competing financial interests or personal relationships that could have appeared to influence the work reported in this paper.

Data availability

No data was used for the research described in the article.

Acknowledgement

We gratefully acknowledge financial support from Business Finland and participating companies (decision number 374/31/2021) within the Towards Fossil-free Steel project as well as from European Union within the Maximise H_2 Enrichment in Direct Reduction Shaft Furnaces project funded by Horizon Europe (grant agreement 101058429). Views and opinions expressed are however those of the author(s) only and do not necessarily reflect those of the European Union. Neither the European Union nor the granting authority can be held responsible for them.

Funded by the European Union

References

Akiyamah, T., Ohta, H., Takahashi, R., Waseda, Y., Yagi, J., 1992. Measurementand oxide and porous modeling of lron ore thermal conductivity for denselron agglomerates in stepwise reduction. ISIJ Int. 7, 829–837. https://doi.org/10.2355/isijinternational.32.829.

Atsushi, M., Uemura, H., Sakaguchi, T., 2010. MIDREX processes. Kobelco Technol. Rev. 29, 50–57.

Bale, C. W., Bélisle, E., Chartrand, P., Decterov, S. A., Eriksson, G., Gheribi, A. E., Hack, K., Jung, I. H., Kang, Y. B., Melançon, J., Pelton, A. D., Petersen, S., Sangster, C.

Robelin. J., Spencer, P., & Van Ende, M.-A., 2016. *FactSage Thermochemical Software and Databases - 2010 - 2016* Calphad, vol 54, pp. 35–53, http://www.factsage.com/.
Bernasowski, M., 2014. Theoretical study of the hydrogen influence on iron oxides reduction at the blast furnace process. Steel Res. Int. 85 (4), 670–678. https://doi.org/10.1002/srin.201300141.
Bonalde, A., Henriquez, A., Manrique, M., 2005. Kinetic analysis of the iron oxide reduction using hydrogen-carbon monoxide mixtures as reducing agent. ISIJ Int. 45 (9), 1255–1260. https://doi.org/10.2355/isijinternational.45.1255.
CHEMCAD v. 7.0, http://www.chemstations.com/.
Chen, Z., Dang, J., Hu, X., Yan, H., 2018. Reduction kinetics of hematite powder in hydrogen atmosphere at moderate temperatures. Metals 8 (10), 751–760. https://doi.org/10.3390/met8100751.
Chen, F., Mohassab, Y., Jiang, T., Sohn, H.Y., 2015. Hydrogen reduction kinetics of hematite concentrate particles relevant to a novel flash ironmaking process. Metall. Mater. Trans. B 46, 1133–1145. https://doi.org/10.1007/s11663-015-0332-z.
El-Geassy, A.A., Nasr, M.I., 1988. Influence of the original structure of hydrogen reduction of hematite on the kinetics compacts. *Trans. Iron Steel Instit.* Japan 28 (8), 650–658. https://doi.org/10.2355/isijinternational1966.28.650.
El-Geassy, A.A., Nasr, M.I., Hessien, M.M., 1996. Effect of reducing gas on the volume change during reduction of iron oxide compacts. ISIJ Int. 3 (6), 640–649. https://doi.org/10.2355/isijinternational.36.640.
Energy Agency, I., 2020. Iron and Steel Technology Roadmap Towards more sustainable steelmaking Part of the Energy Technology Perspectives series. https://www.iea.org/t&c.
Gao, X., Shen, J., Hsias, Y., Chen, Y., 1993. Reduction of supported iron oxide studied by temperature-programmed reduction combined with mossbauer spectroscopy and X-ray diffraction. J. Chem. Soc., Faraday Trans. 89 (7), 1079–1084. https://doi.org/10.1039/FT9938901079.
Hammam, A., Li, Y., Nie, H., Zan, L., Ding, W., Li, M., Omran, M., Yu, Y., 2021. Isothermal and non-isothermal reduction behaviors of iron ore compacts in pure hydrogen atmosphere and kinetic analysis. Mining, Metall. Explor. 38, 81–93. https://doi.org/10.1007/s42461-020-00317-3.
Hara, Y., Tsuchiya, M., Kondo, S., 1974. Intraparticle temperature of iron-oxide pellet during the reduction. Tetsu-to-Hagane 60 (9), 1261–1270. https://doi.org/10.2355/tetsutohagane1955.60.9_1261.
Hessling, O., Brännberg, J., Fogelström, M., Kojola, N., Sichen, D., 2022. The effect of the endothermic reaction nature on the iron ore pellet reduction using hydrogen. Metall. Mater. Trans. B 52, 1258–1268. https://doi.org/10.1007/s11663-023-02908-z.
Hou, B., Zhang, H., Li, H., Zhu, Q., 2012. Study on kinetics of iron oxide reduction by hydrogen. Chin. J. Chem. Eng. 20 (1), 10–17. https://doi.org/10.1016/S1004-9541(12)60357-7.
Hutny, W.P., Lee, G.K., Price, J.T., 1991. Fundamentals of coal combustion during injection into a blast furnace. Prog. Energy Combust. Sci. 17 (4), 373–395.
Jess, A., Depner, H., 1998. Reduction and carburization of iron-ore in a fluidized bed by CO, H2 and CH4. Steel Res. 69, 77–84. https://doi.org/10.1002/srin.199801454.
Jozwiak, W.K., Kaczmarek, E., Maniecki, T.P., Ignaczak, W., Maniukiewicz, W., 2007. Reduction behavior of iron oxides in hydrogen and carbon monoxide atmospheres. *Appl. Catal., A*: *General* 326 (1), 17–27. https://doi.org/10.1016/j.apcata.2007.03.021.
Kazemi, M., Pour, M.S., Sichen, D., 2017. Experimental and modeling study on reduction of hematite pellets by hydrogen gas. Metall. Mater. Trans. B 48 (2), 1114–1122. https://doi.org/10.1007/s11663-016-0895-3.
Lin, H.Y., Chen, Y.W., Li, C., 2003. The mechanism of reduction of iron oxide by hydrogen. Thermochim. Acta 400 (1–2), 61–67. https://doi.org/10.1016/S0040-6031(02)00478-1.
Mauret, F., Baniasadi, M., Saxén, H., Feiterna, A., Hojda, S., 2023. Impact of hydrogenous gas injection on the blast furnace process: a numerical investigation. Metall. Mater. Trans. B 54 (4), 2137–2158. https://doi.org/10.1007/s11663-023-02822-4.
Oh, J., Noh, D., 2017. The reduction kinetics of hematite particles in H2 and CO atmospheres. Fuel 196, 144–153. https://doi.org/10.1016/j.fuel.2016.10.125.
Patisson, F., Mirgaux, O., Birat, J.P., 2021. Hydrogen steelmaking. Part 1: physical chemistry and process metallurgy. Mater. Tech. 109 (3–4) https://doi.org/10.1051/mattech/2021025.
Pineau, A., Kanari, N., Gaballah, I., 2006. Kinetics of reduction of iron oxides by H2. Part I: low temperature reduction of hematite. Thermochim. Acta 447 (1), 89–100. https://doi.org/10.1016/j.tca.2005.10.004.
Piotrowski, K., Mondal, K., Lorethova, H., Stonawski, L., Szymański, T., Wiltowski, T., 2005. Effect of gas composition on the kinetics of iron oxide reduction in a hydrogen production process. Int. J. Hydrogen Energy 30 (15), 1543–1554. https://doi.org/10.1016/j.ijhydene.2004.10.013.
Rahmatmand, B., Tahmasebi, A., Lomas, H., Honeyands, T., Koshy, P., Hockings, K., & Jayasekara, A., 2023. A technical review on coke rate and quality in low-carbon blast furnace ironmaking. *Fuel* (Vol. 336). Elsevier Ltd. https://doi.org/10.1016/j.fuel.2022.127077.
Shao, L., Xu, J., Saxén, H., Zou, Z.-S., 2023. A numerical study on process intensification of hydrogen reduction of iron oxide pellets in a shaft furnace. Fuel 348, 128375. https://doi.org/10.1016/j.fuel.2023.128375.
Spreitzer, D., Schenk, J., 2019. Iron ore reduction by hydrogen using a laboratory scale fluidized bed reactor: kinetic investigation—Experimental setup and method for determination. Metall. Mater. Trans. B 50 (5), 2471–2484. https://doi.org/10.1007/s11663-019-01650-9.
Szekely, J., Evans, J.W., 1970. A structural model for gas-solid reactions with a moving boundary. Chem. Eng. Sci. 25 (6), 1091–1107. https://doi.org/10.1016/0009-2509(70)85053-9.
Takahashi, R., Yagi, J., Omori, Y., 1971. Reduction rate of iron oxide pellets with hydrogen. Phys. Chem. Metals 9–30.
Wei, Z., Zhang, J., Qin, B., Dong, Y., Lu, Y., Li, Y., Hao, W., Zhang, Y., 2018. Reduction kinetics of hematite ore fines with H2 in a rotary drum reactor. Powder Technol. 332, 18–26. https://doi.org/10.1016/j.powtec.2018.03.054.
Zhang, W., Zhang, J., Li, Q., He, Y., Tang, B., Li, M., Zhang, Z., Zou, Z., 2013. Thermodynamic analyses of iron oxides redox reactions. In: Marquis, F. (Ed.), Proceedings of the 8th Pacific Rim International Congress on Advanced Materials and Processing. Springer, Cham, pp. 777–789. https://doi.org/10.1007/978-3-319-48764-9_96.
Zuo, H., Wang, C., Dong, J., Jiao, K., Xu, R., 2015. Reduction kinetics of iron oxide pellets with H2 and CO mixtures. Int. J. Miner. Metall. Mater. 22 (7), 688–696. https://doi.org/10.1007/s12613-015-1123-x.